Pergamon

Geochimica et Cosmochimica Acta, Vol. 68, No. 11, pp. 2517–2527, 2004

0016-7037/04 $30.00 + .00

doi:10.1016/j.gca.2003.10.042

Microstructure of 24-1928 Ma concordant monazites; implications for geochronology and nuclear waste deposits

ANNE-MAGALI SEYDOUX-GUILLAUME,[1,*,†] RICHARD WIRTH,[2] ALEX DEUTSCH,[1] and URS SCHÄRER[3]

[1]Institut für Planetologie, Wilhelm-Klemm-Str. 10, Westfälische Wilhelms-Universität Münster (WWU), D-48149 Münster, Germany
[2]GeoForschungsZentrum (GFZ) Potsdam-Division 4, Telegrafenberg, D-14473 Potsdam, Germany
[3]Géosciences Azur, CNRS-UMR 6526, Université de Nice-Sophia Antipolis, Parc Valrose, F-06108 Nice, France

(*Received June* 10, 2003; *accepted in revised form October* 27, 2003)

Abstract—The microstructure of monazite was studied using scanning electron microscopy (SEM), electron microprobe analysis (EMP), X-ray diffraction patterns (XRD), and transmission electron microscopy (TEM). Four well-characterized monazites were investigated, having very different concordant U-Pb ages (24 to 1928 Ma), and up to ~15 wt.% ThO_2, and ~0.94 wt. % UO_2. The SEM and EMP analyses of polished single crystal fragments reveal the absence of significant chemical zoning. XRD and TEM investigations show that the monazites are not metamict, despite their old ages, very high abundances of radionuclides, and hence, high time-integrated radiation doses. Except for the youngest one, the monazite crystals are composed of a mosaic of crystalline but slightly distorted domains. This structure is responsible for the presence of (1) mottled diffraction contrasts on the TEM, and (2) a second structural phase (B), with very broad reflections in the XRD patterns. Older monazites receive higher self-irradiation doses, and hence, they contain higher amounts of this B-phase. For the 1928 Ma monazite, XRD reveals only the broad reflections of phase B, implying that the whole monazite was affected by radiation damage that resulted in total distortion of the lattice. It is concluded that radiation damage in the form of amorphous domains does not accumulate in monazite because self-annealing heals the defects as they are produced by α-decay damage. The only memory of irradiation-induced defects is the presence of distorted domains. As the diffusion rate of Pb in an undisturbed monazite lattice is extremely low, Pb loss due to volume diffusion out of the monazite lattice is virtually impossible. This is considered as one reason why almost all monazites have concordant U-Th-Pb ages. Moreover, as long-term self-irradiation effects are limited in monazite, we consider this phase as a good candidate for the storage of high-level nuclear waste under the aspect of its high resistance to irradiation.

1. INTRODUCTION

The accessory mineral monazite is a natural light rare earth orthophosphate (APO_4: A = LREE, Th, U, Ca, Pb) that contains high concentrations of U and Th (up to 6 wt.% UO_2 and 20 wt.% ThO_2; e.g., Montel et al., 1996; Förster, 1998; Seydoux-Guillaume et al., 2002a). Monazites are widely used in U-Pb geochronology because of their high actinide and low common Pb contents (Parrish, 1990). In contrast to zircon, monazite mostly gives concordant U-Pb ages (e.g., Köppel, 1974; Schärer et al., 1986; Corfu, 1988; Smith and Barreiro, 1990; Parrish, 1995; Landzirotti and Hanson, 1995), indicating that the U-Pb systems of the monazites are either completely reset or remain totally unaffected during most geological events. Nevertheless, some discordant U-Pb ages have also been reported. Most of these may be explained by the analysis mixtures of newly grown rims and inherited cores (e.g., Cocherie et al., 1998; Paquette et al., 1999; Krohe and Wawrzenitz, 2000; Goncalves, 2002; Paquette et al., 2003; Seydoux-Guillaume et al., 2003) and diffusive Pb loss is assumed only in rare cases (Suzuki and Adachi, 1994; Suzuki et al., 1994). To understand the geological significance of monazite ages measured, one needs to understand the mechanism of resetting the U-Pb system in this phase.

Two processes are commonly considered to explain resetting of the U-Pb isotopic system: (1) Pb loss by volume diffusion out of the grain or (2) dissolution of the crystal by a fluid, followed by precipitation of a newly formed Pb-free crystal (Teufel and Heinrich, 1997; Seydoux-Guillaume et al., 2002b). With respect to process (1), there have been several attempts to interpret discordant ages of monazites in terms of Dodson's (1973) closure temperature model. In this model, resetting results from the diffusion of daughter isotopes out of the crystal. The assumed closure temperature depends on the size of the crystal, its shape, the cooling rate, and the diffusion coefficient of the daughter elements. Experiments on Pb diffusion by Smith and Giletti (1997) and Cherniak et al. (2000), however, showed that this diffusion is very slow in monazite, even at high temperatures. A different approach is to determine an empirical "geological closure temperature" using isotopic ages of different minerals combined with petrologically derived temperatures for metamorphic events. This method yielded temperature estimates as low as 530 ± 25°C (Black et al., 1984) to 725 ± 25°C (Copeland et al., 1988). It has been shown, however, that monazite inclusions that were shielded by host minerals such as quartz or garnet still retain "old" ages, despite annealing under granulite-facies conditions at temperatures above 800°C over longtime scales (De Wolf et al., 1993; Kalt et al., 2000; Montel et al., 2000). Such observations raise the question of whether diffusion is the main resetting mech-

* Address reprint requests to A. M. Seydoux-Guillaume, LMTG-UMR 5563, 14 avenue Edouard Belin, 31400 Toulouse, France (seydoux@lmtg.obs-mip.fr).
† *Present address:* A.M. Seydoux-Guillaume, LMTG-UMR 5563, 14 avenue Edouard Belin, 31400 Toulouse, France.

anism. An alternative mechanism is dissolution/precipitation. This is the only resetting mechanism for the U-Pb system in monazites detected in the experiments of Teufel and Heinrich (1997) and Seydoux-Guillaume et al. (2002b). The extent of the dissolution/precipitation process depends on the fluid composition (Seydoux-Guillaume et al., 2002b) and is a more efficient mechanism for resetting than lead loss by volume diffusion.

In minerals relevant for U-Pb dating, radioactive decay produces radiation damage that may partially or totally destroy the crystal lattice, thus producing so-called metamict domains. Whatever the mechanism of resetting is, the kinetics of resetting are strongly influenced by the degree of metamictization of the crystal. This structural state is essential, as physical properties of an amorphous phase differ significantly from those of its crystalline counterpart (e.g., Weber et al., 1998; Ewing et al., 2000). It was suggested that Pb diffusion is enhanced in a metamict crystal (Cherniak, 1993) and radiogenic Pb diffuses much faster within "channels" that correspond to the percolating interface between amorphous and crystalline domains (e.g., Salje, 2000; Trachenko et al., 2000; Geisler et al., 2002). Moreover, radiogenic Pb can be leached more easily from a damaged lattice (Davis and Krogh, 2000; Romer, 2003). Consequently, a damaged lattice will retain radiogenic Pb to a lesser degree than a perfect one, resulting in discordant ages for phases that exist in such a structural state. As pointed out by Villa (2002), microstructural investigations are, therefore, of fundamental importance to better understand isotopic ages of minerals.

Characterising the structural state of U- and Th-rich phases is essential when considering their potential use in nuclear waste deposit strategies. Monazite-based ceramics have been first proposed by Boatner et al. (1980) as a crystalline matrix for immobilizing radionuclides, especially the actinides. This concept is currently the focus of research on nuclear waste deposit strategies (e.g., Poitrasson et al., 1996, 2000; Read and Williams, 2001; Oelkers and Poitrasson, 2002; Montel et al., 2002; Poitrasson et al., 2002). The advantage of studying natural monazites in this context is that this mineral provides data on the response of the lattice to irradiation over geologic timescales at very low dose rates ($<10^{-17}$ dpa/s; Weber et al., 1998). In contrast, studies using actinide-doped phases (10^{-10}-10^{-8} dpa/s) or charged-particle irradiation (10^{-5}-10^{-2} dpa/s; Weber et al., 1998) simulate very high dose rates, but only over short time periods.

Monazite receives intense self-irradiation doses during its geologic history because of its generally high U and Th contents. During an α-decay event, a radionuclide liberates its energy by ejecting an α-particle while the remaining nucleus is recoiled in the opposite direction. Most of the atomic displacements that result in amorphization of a crystal lattice are caused by α-recoil nuclei (e.g., Ewing, 1995; Nasdala et al., 1996; Weber et al., 1998; Ewing et al., 2000). Up to now, monazite was rarely found in the metamict state despite the fact that it generally experienced intensive radiation doses (Ewing, 1975), and clear evidence of radiation damage was limited to isolated nm-sized domains within the crystal (Black et al., 1984; Meldrum et al., 1998; Seydoux-Guillaume et al., 2002c). Seydoux-Guillaume et al. (2002c) were the first to study a monazite in detail by using various complementary analytical methods, including X-ray diffraction (XRD), transmission electron microscopy (TEM), Raman, and cathodoluminescence. The studied monazite was a chemically homogeneous Brazilian monazite (called Moacir) that yielded a concordant U-Pb age of 474 Ma and a U-Th/He age of 479 Ma. This monazite also showed nm-scale defects induced by α-decay. The new result of this study, revealed by the XRD technique, is the presence of two distinct monazite "phases," A and B, that have different lattice parameters. Because monazite A shows sharp reflections of high amplitude and larger lattice parameters, it was interpreted to be well-crystallized monazite that had an expanded lattice as a result of Helium accumulation. As monazite B exhibits very broad, low amplitude reflections, it was interpreted to be a Helium-free distorted monazite crystal lattice, which can be attributed to old α-recoil tracks.

The results of the study by Seydoux-Guillaume et al. (2002c) prompted new questions: Will this phenomenon be visible in other monazites? Is there a correlation between the B domains, the U, Th contents of the monazites, and hence, the self-irradiation dose received by monazite?

To address these questions, we performed a comparative study of four well-dated monazites (Table 1). They were selected for the following reasons: (1) all have concordant U-Pb ages (Schärer and Deutsch, 1990; Paquette et al., 1994; Schärer et al., 1994; Seydoux-Guillaume et al., 2002b). Hence, we can exclude recent alteration events that would complicate data interpretation; (2) their ages range from 24 to 1928 Ma; (3) the contents of radionuclides vary widely, reaching up to ~15 wt.% ThO_2 and up to ~0.94 wt.% UO_2. It follows from (2) and (3) that: (4) these monazites received quite different self-irradiation doses, ranging from 0.13 to 17×10^{19} α-decay/g. Using essentially XRD and TEM techniques, we investigated the micro-nanostructure of these monazites. The final aim of this study is to compare the effects of long-term self-irradiation in these monazites over a wide range of α-decay doses to specify implications for U-Pb geochronology and nuclear waste storage.

2. SAMPLES (TABLE 1)

2.1. YS35

The youngest monazite YS35 comes from a garnet-biotite leucogranite layer in the Diancang Shan Gneisses from the Red River Belt, China. The monazites YS35 have concordant U-Pb ages of 24.2 Ma (Schärer et al., 1994). A large series of U-Pb dating results from various accessory minerals (Schärer et al., 1994; Zhang and Schärer, 1999), some $^{40}Ar/^{39}Ar$ data from micas, and a modelled Ar degassing pattern of K-Fsp from the Ailao-Shan-Red River shear zone (Leloup et al., 1995) show that this belt cooled rapidly after granitic-alkaline magmatism and high-strain ductile deformation, reaching the 300°C isograd at 20–19 Ma. This fast cooling was followed by a very inactive period of ~15 m.y. during which the gneisses remained at ~300°C. Final cooling occurred after ~4 Ma during exhumation and erosion of the gneiss that was associated with dextral strike-slip shear along what is the presently active Red River fault. These monazites are ~200 × 400 μm large and transparent yellow grains.

Table 1. Monazites used in this study.

#		YS35	Moacir	Madagascar	DIG19
Geological context		Garnet-biotite leucogranite Diancang Shan Red River Belt China	Pegmatite from Itambé Province Brazil	Apatitite from Anosyan granite, Manangotry Madagascar	Felsic high grade metamorphic Gneiss, Devon Island, Sverdrup Inlet (Canada)
U-Pb age (Ma)[a]		24 Schärer et al. (1994)	474 Seydoux-Guillaume et al. (2002b)	545 Paquette et al. (1994)	1928 Schärer and Deutsch (1990)
SEM		lightly zoned	homogeneous	homogeneous	lightly zoned
Chemical composition (wt.%)	ThO_2	5.74–15.60	6.92	13.25	9.03–10.33
	UO_2	0.29–0.94	0.13	0.20	0.14–0.46
	PbO	~0–0.05	0.16	0.32	0.76–0.95
Theoretical dose	α/g[b]	0.13×10^{19}	2.77×10^{19}	6.12×10^{19}	17×10^{19}
	dpa[c]	0.12	2.32	5.13	14.20
XRD		*	2 reflections; one sharp (A) and one broad (B) B $\approx$ A	2 reflections; one sharp (A) and one broad (B) B > A	an unique and broad reflection (B) B $\gg$ A
	BF	small amount of mottled diffraction contrasts (few spots)	large amount of mottled diffraction contrasts (many spots ~ 5 nm size)	large amount of mottled diffraction contrasts size ~ 10 nm	large amount of mottled diffraction contrasts size ~ 80 nm
TEM	SAD		SAD patterns always show sharp reflections		
	HREM	defects not detectable	few isolated distorded areas	few isolated distorded areas	many isolated distorted areas (edge dislocations)

[a] Concordant ages; determination by the isotope dilution technique.
[b] Doses calculated with equation in Nasdala et al. (2001).
[c] Displacement per atom. Calculated after Meldrum et al. (1998) with a number of atom displacement per α-decay (n) of 860.
* Available amount of sample too small for XRD investigations.

2.2. Moacir

The second monazite, Moacir, is a large (centimeter-sized) yellow-orange single crystal from a pegmatite in the Itambé Province, Brazil (Cruz et al., 1996). It has a concordant U-Pb age of 474 Ma (Seydoux-Guillaume et al., 2002b) and a U-Th/He age of ~ 479 Ma (R. Pik, private communication). Moacir is the reference monazite for this study as it has been previously characterized using SEM, EMP, XRD, TEM, Raman microprobe, and cathodoluminescence techniques (Nasdala et al., 2002; Seydoux-Guillaume et al., 2002c).

2.3. Madagascar

The third monazite, Madagascar, is a yellow, centimeter-sized, single crystal that has given concordant U-Pb ages of 545 Ma (Paquette et al., 1994). A U-Th/He analysis yielded an identical age (R. Pik, private communication) indicating that, like for Moacir, all helium produced by α-decay during the existence of the crystal is essentially still present in the monazite lattice. This monazite was separated from an apatitite from the Anosyan granites, Madagascar.

2.4. DIG19

The oldest monazite, DIG19, comes from exceptionally fresh, felsic high-grade metamorphic gneiss from Sverdrup Inlet, Devon Island, N.W.T., Canada. It gave concordant U-Pb ages of 1928 Ma (Schärer and Deutsch, 1990). A biotite-feldspar-whole rock Rb-Sr isochron of this gneiss corresponds to an age of 1814 ± 8 (Schärer and Deutsch, 1990). The high-grade crystalline basement is covered by Proterozoic metasediments, upon which undeformed and unmetamorphosed Cambrian to Devonian sediments rest unconformably. This simple geology indicates that the DIG19 monazites remained in the upper crust at low temperature for at least 540 Ma. The monazite crystals are yellow and typically 100 × 100 μm in size.

3. ANALYTICAL METHODS

3.1. Scanning Electron Microscope (SEM) and Electron Microprobe (EMP)

All monazite grains were individually mounted in epoxy, polished, and carbon coated in preparation for imaging by back-scattered electron (BSE) and secondary electron (SE) techniques. Images were acquired using the JEOL JSM-840A SEM at the Institut für Planetologie, WWU Münster. Acceleration voltage was typically 20 kV.

The EMP analyses were obtained using the CAMECA SX-50 electron microprobe at the GFZ-Potsdam, equipped with a wavelength dispersive spectrometer. The operating conditions were: accelerating potential 20 kV, beam current 40–60 nA, and 1–2 μm beam diameter. For details, see Förster et al. (1998).

3.2. X-ray Diffraction (XRD)

About 1 mg of powdered monazite was measured in transmission mode using the fully automated STOE STADI P diffractometer (Cu-Kα_1 radiation) equipped with a primary monochromator and a 7°-position sensitive detector (PSD) at the GFZ-Potsdam. Details are given in Seydoux-Guillaume et al. (2002c). Two kinds of diffraction patterns were recorded. One pattern spanned from 5 to 125° (2θ) with a step size of 0.01°. The intensity was counted for 135 s at each position. The second pattern covered the 2θ range between 26 and 28°

with the same step size and a counting time of 1000 s per detector step. The unit-cell refinements were performed using the Rietveld-refinement program of the GSAS software package (Larson and Von Dreele, 1988). The XRD patterns in the range of 26–28° (2θ) were fitted by a Gauss + Lorentz area function to determine the full width at half maximum (FWHM), areas, and the maximum position of the (200) reflection.

Monazite YS35 was not studied by XRD due to the insufficient amount of sample material.

3.3. Transmission Electron Microscope (TEM)

The YS35, Moacir, and Madagascar monazites were cut in random orientation, and TEM foils were prepared by hand polishing and argon ion milling at 5 kV (Institut für Planetologie, WWU Münster). Due to its very small size, the DIG19 monazite was prepared using the Focused Ion Beam technique FEI FIB200 at the GFZ-Potsdam. For both thinning techniques, particular care was taken to avoid artificial defect production by the ion beam during milling. For the conventional Ar-milling technique, Seydoux-Guillaume et al. (2002c) demonstrated by preparing both untreated and annealed (at 1000°C) samples, that the observed defects are not artefacts from the milling process. Black et al. (1984) demonstrated early on that TEM analysis of crushed monazite fragments and ion-thinned foils give the same results. For the FIB technique, results are the same. The gallium beam used in the FEI FIB200 is responsible for implantation of gallium ions during milling, causing gallium peaks in Energy Dispersive Spectroscopy (EDS) analyses, and creates a ~20 nm amorphous layer near the surface. However, the latter phenomenon does not adversely affect the observations.

The TEM studies were carried out using the Philips CM 200 TEM at the GFZ-Potsdam operated at 200 kV and the JEOL 3010 TEM at the Institut für Planetologie, WWU Münster operated at 300 kV. Both instruments are equipped with a LaB_6 electron source. High-resolution TEM (HRTEM) images were acquired as energy filtered images applying a 10 eV window to the zero-loss peak using a Gatan GIF^{TM} system. Bright Field images (BF) of all samples were done close to a zone axis, i.e., where a maximum contrast is present, allowing direct comparison of the results.

4. RESULTS

All results are compiled in Table 1. Data for the reference monazite Moacir are from Nasdala et al. (2002) and Seydoux-Guillaume et al. (2002a, b, and c).

4.1. Chemical Composition of the Monazites (SEM and EMP)

The BSE micrographs show that the Moacir and Madagascar monazites are chemically homogeneous (Figs. 1a and b), whereas, monazites YS35 and DIG19 display a vague zoning (Figs. 1c and d).

The EMP analytical results are compiled in Table 2. The four monazites have different chemical compositions. Importantly, they show large variations in their actinide and lead contents: The ThO_2 content ranges from ~6 to 15 wt.%, the UO_2 content from ~0.13 to ~0.94 wt. %, and the PbO content amounts up to ~0.95 wt. % (Tables 1 and 2). The Moacir and the Madagascar monazites have approximately the same age, but very different U and Th contents; hence, they have received different irradiation doses. The chemical homogeneity of the Moacir and Madagascar monazites was investigated by Seydoux-Guillaume et al. (2002a, b, and c); therefore, only representative analyses of these monazites is given in Table 2.

Using actinide contents and U-Pb ages, we calculated the theoretical self-irradiation doses of the monazites (e.g., Nasdala et al., 2001). These doses, compiled in Table 1, correspond to the number of α-decay events that have occurred during the geologic history of the respective monazite. The self-irradiation dose increases from 0.13×10^{19} α-decay/g for the youngest monazite YS35, over 2.77×10^{19} α-decay/g for the Moacir monazite, 6.12×10^{19} α-decay/g for the Madagascar monazite, to 17×10^{19} α-decay/g for DIG19, the oldest monazite. For comparison, estimated doses for some well-studied zircon samples amount to only 1×10^{19} α-decay/g (e.g., Holland and Gottfried, 1955; Murakami et al., 1991; Ewing et al., 2000; Nasdala et al., 2002). Ceramics, doped with 1 wt.% ^{239}Pu, will receive a dose of $\sim 10 \times 10^{19}$ α-decay/g in 100 000 yrs (Weber et al., 1998).

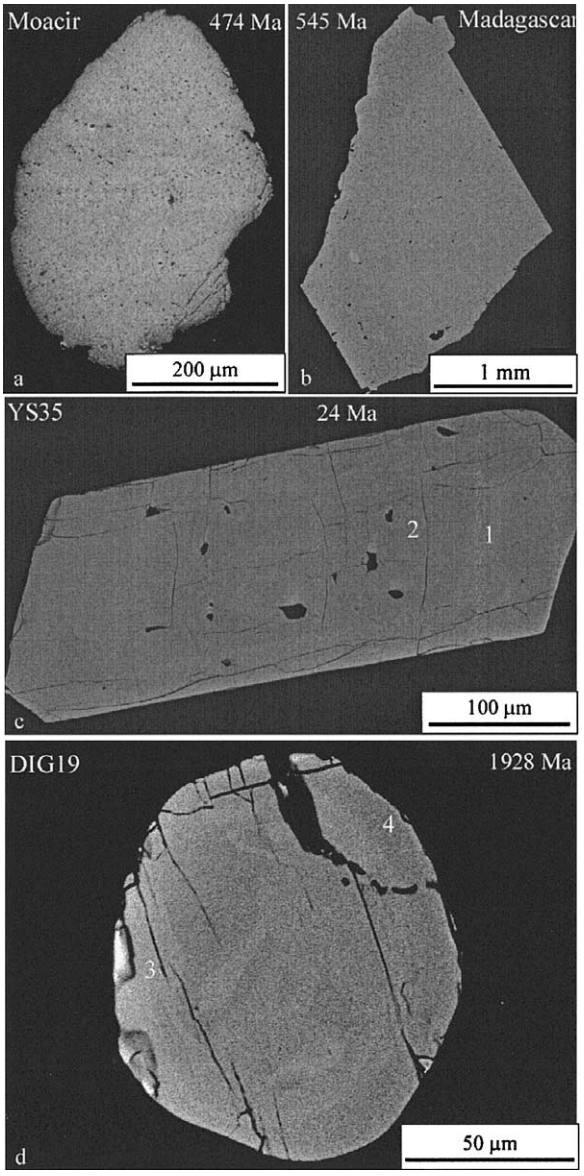

Fig. 1. BSE images of different monazite crystals: a) Moacir, b) Madagascar, c) YS35 and d) DIG19. Both monazites a and b are chemically homogeneous and the two others (c and d) are slightly zoned.

Table 2. Electron Microprobe (EMP) analyses of the four monazites.

	YS35				DIG19	
Oxides (wt. %)	1* (bright)	2 (dark)	Moacir	Madagascar	3 (bright)	4 (dark)
P_2O_5	25.82	28.33	27.81	26.46	29.44	27.61
SiO_2	2.65	1.19	1.42	2.22	0.52	1.47
ThO_2	13.26	7.52	6.92	13.25	9.07	10.32
UO_2	0.63	0.40	0.13	0.20	0.37	0.14
Y_2O_3	2.30	2.06	0.71	0.18	0.04	0.24
La_2O_3	10.68	11.31	14.51	14.04	12.10	11.56
Ce_2O_3	23.05	25.38	30.59	28.79	28.89	28.61
Pr_2O_3	2.69	3.00	3.14	2.72	3.18	3.22
Nd_2O_3	11.11	12.38	10.20	9.15	11.76	12.60
Sm_2O_3	3.17	3.88	2.05	0.95	1.45	1.35
Gd_2O_3	2.53	2.73	0.94	0.39	0.50	0.72
Tb_2O_3	0.26	0.27	–	–	0.00	0.00
Dy_2O_3	0.50	0.52	0.11	0.01	0.00	0.00
Ho_2O_3	0.02	0.07	–	–	0.00	0.00
Er_2O_3	0.11	0.11	0.05	0.03	0.00	0.00
Yb_2O_3	0.04	0.01	–	–	0.02	0.00
Lu_2O_3	0.00	0.00	–	–	0.00	0.00
PbO	0.00	0.02	0.16	0.32	0.95	0.85
CaO	0.67	0.80	0.44	1.03	1.69	0.89
Σ	99.50	99.98	99.18	99.74	99.96	99.58

* Numbers referred to Fig. 1c and d.

4.2. Structural Observations (XRD and TEM)

4.2.1. X-ray diffraction analysis

The X-ray diffraction patterns of the monazites Moacir, Madagascar, and DIG 19 are characterized by relatively sharp reflections of relatively high intensities. As shown in Figure 2a, the reflections broaden for the monazites with a higher self-irradiation dose, while the peak to background ratio decreases. Some reflections display a shoulder on the flank towards higher 2θ values (arrows in Fig. 2a). The number of these shoulders (arrows in Fig. 2a) decreases with higher self-irradiation doses due to the increased broadening of the peaks. In their study of the Moacir monazite, Seydoux-Guillaume et al. (2002c) pointed out that this broadening is most pronounced along (200) reflection, i.e., at 2θ diffraction angles of 26 to 28°. Therefore, we obtained high-resolution X-ray diffraction patterns in this range for the two other monazites as well. (Fig. 2b).

A typical diffraction pattern in the 2θ range of 26–28° is given for the Moacir monazite in Figure 2b. It shows one characteristic reflection (A) of high amplitude that is very sharp (FWHM = 0.091°) and, additionally, a broad (FWHM = 0.425°) shoulder (B) of low amplitude (Table 3). The B-reflection maximum is located at the 2θ value of 27.04° (3.295Å) whereas the maximum of the A-reflection is located at 26.88° (3.314 Å; Table 3). The area percentage of A and B reflections are 47 and 53%, respectively (Table 3). Rietveld-refinement of the XRD data for the unheated monazite, assuming only a single-phase (A) with a monazite structure, failed. Introducing a second phase (B, monazite structure assumed), however, resulted in a successful Rietveld refinement. Consequently the XRD patterns are interpreted to consist of two phases, both having monazite structure but with different lattice parameters (Table 3). Monazite (A) shows larger lattice parameters (1% in volume) than the synthetic reference crystal $CePO_4$ from Ni et al. (1995). The lattice parameters of monazite (B), however, correspond well to those of this reference crystal.

Like the Moacir monazite, the X-ray pattern of the Madagascar monazite consists of the two structurally distinct monazite phases A and B with slightly different lattice parameters (Table 3). Phase A shows sharp reflections with $FWHM_{(200)}$ of 0.088°. Phase B, in contrast, exhibits very broad reflections with $FWHM_{(200)}$ of 0.336° and an amplitude lower than that of phase A (Table 3). In the case of the Madagascar monazite, the integrated area under the B-reflection, ~80% for the (200) peak, is larger than for the Moacir monazite, where we observe only ~53% for (200). Thus, the contribution of the B-reflections is larger in the Madagascar compared to the Moacir monazite. In addition, the A-reflection maximum for the Madagascar monazite is shifted towards lower 2θ values compared to the Moacir monazite.

In contrast to the other monazites, monazite DIG19 shows only one reflection. This reflection is very broad ($FWHM_{(200)}$ = 0.276°) and has its maximum at a 2θ value close to the maximum reflection of phase B in the Moacir and Madagascar monazites.

4.2.2. TEM-Bright Field (BF) images

All four monazites show mottled diffraction contrasts in their BF images, but with significant differences among them (Fig. 3). The young YS35 monazite displays just a few, spot-like contrasts (Fig. 3a), indicating that monazite YS35 is an almost perfect crystal. The Moacir monazite has many mottled diffraction contrasts. The areas showing these contrasts are larger (~5 nm-sized domains) and appear to be more frequent compared to those of the YS35 monazite (Fig. 3b). This effect is even more pronounced in the Madagascar monazite (Fig. 3c) where the domains are again larger (~10 nm across) than in the Moacir

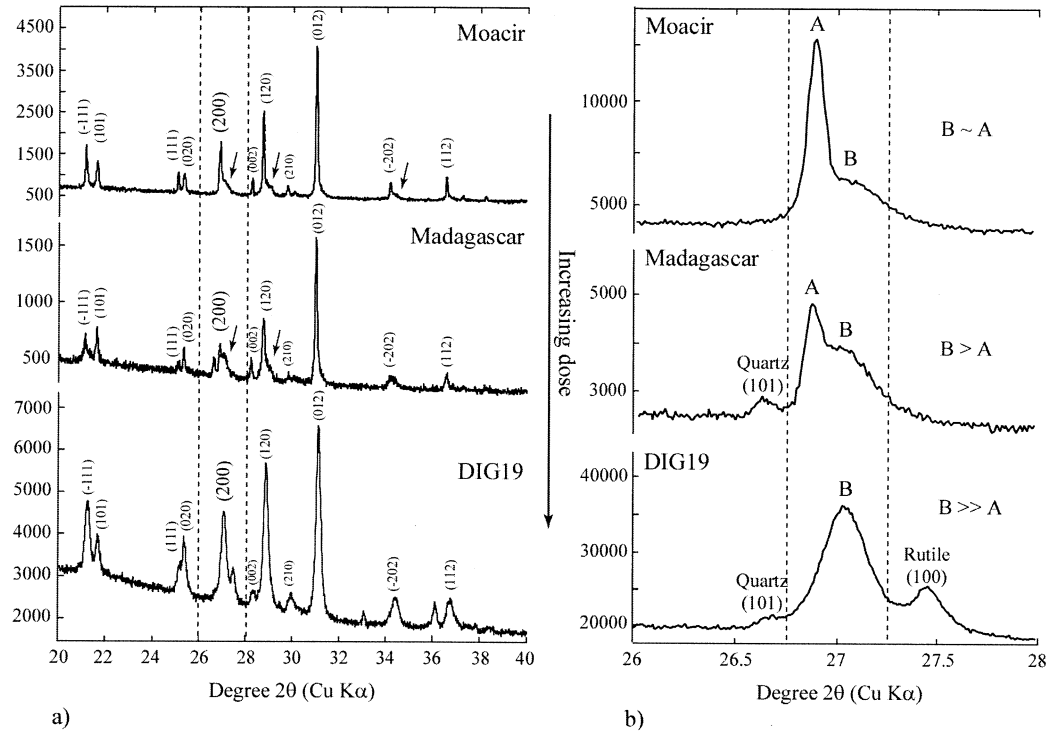

Fig. 2. XRD patterns of the three monazites Moacir, Madagascar and DIG19 in the 2θ range of: a) 20 to 40°. The reflections broaden with increasing self-irradiation dose. However, the monazites are not yet amorphous. [Peak intensity-Background intensity] ratio decreases with increasing dose. Note the presence of a shoulder on the high 2θ side of some reflections (arrows). The number of these shoulders decreases with increasing dose due to the increasing broadening of the reflections. b) 26 to 28°, corresponding to the (200) reflection of the monazites. Two structurally different phases A (well-crystallized monazite, sharp reflections) and B (distorted monazite, broad reflections) were distinguished for the Moacir and the Madagascar monazites. Monazite DIG19 shows only the broad B reflection (see X-Ray data in Table 3).

monazite. Finally, monazite DIG19 (Fig. 3d) shows very large domains (~80 nm across) of mottled diffraction contrasts. These patterns are very similar to the TEM dark field images published by Black et al. (1984). All these mottled diffraction contrasts are the result of a mosaic structure of the crystal, i.e., a lattice comprising many smaller domains that have slightly different orientations. The dark areas represent domains oriented close to a zone axis, and the bright ones are regions that are not diffracting.

4.2.3. *Selected area diffraction (SAD) and HRTEM observations*

The SAD patterns of all studied monazites (Fig. 4, inserts a1, b1, c1, and d1) show sharp reflections. Evidence for amorphous rings or distorted reflections is lacking. The HRTEM image of monazite YS35 shows neither defects, nor distorted domains. The lattice is almost perfect (Fig. 4a). The Moacir and Madagascar monazites revealed some isolated *ca.* 5 nm^2-sized areas where the lattice fringes were blurred (Figs. 4b and c). The distorted areas impose a local strain on the lattice, causing an inhomogeneous contrast distribution. As illustrated in the Inverse Fourier Transform images (IFFT) of Figures 4b2 and c2, these domains correspond to regions where the lattice is distorted. Finally, the HRTEM image of monazite DIG19 (Fig. 4d) displays contrasts comparable to those of the Moacir and Madagascar monazites, but the IFFT image shows edge dislocations (Fig. 4d2; see arrow). In this monazite, the domains seem to be more distorted than in the other monazites.

Table 3. Compilation of X-ray diffraction data for two domains A and B in the investigated monazites.

		a (Å)	*b* (Å)	*c* (Å)	β (Å)	*V* (Å^3)	FWHM*$_{(200)}$ (°2θ)	Peak position (200) (°2θ)	% Area (200)
A**	Moacir	6.823 (1)	7.026 (1)	6.499 (1)	103.79 (1)	302.60 (9)	0.091 (1)	26.88	47
	Madagascar	6.827 (2)	7.027 (2)	6.508 (1)	103.87 (2)	303.08 (17)	0.088 (3)	26.86	20
	DIG19	–	–	–	–	–	–	–	0
B**	Moacir	6.783 (5)	7.014 (6)	6.489 (5)	103.69 (9)	299.98 (36)	0.425 (6)	27.04 (1)	53
	Madagascar	6.784 (6)	7.016 (4)	6.492 (5)	103.64 (8)	300.32 (36)	0.336 (13)	27.01 (1)	80
	DIG19	6.788 (2)	7.010 (2)	6.491 (2)	103.73 (2)	300.04 (20)	0.276 (2)	27.04	100

* FWHM = Full Width at Half Maximum.
** A corresponds to the crystalline areas and B to the distorted areas.

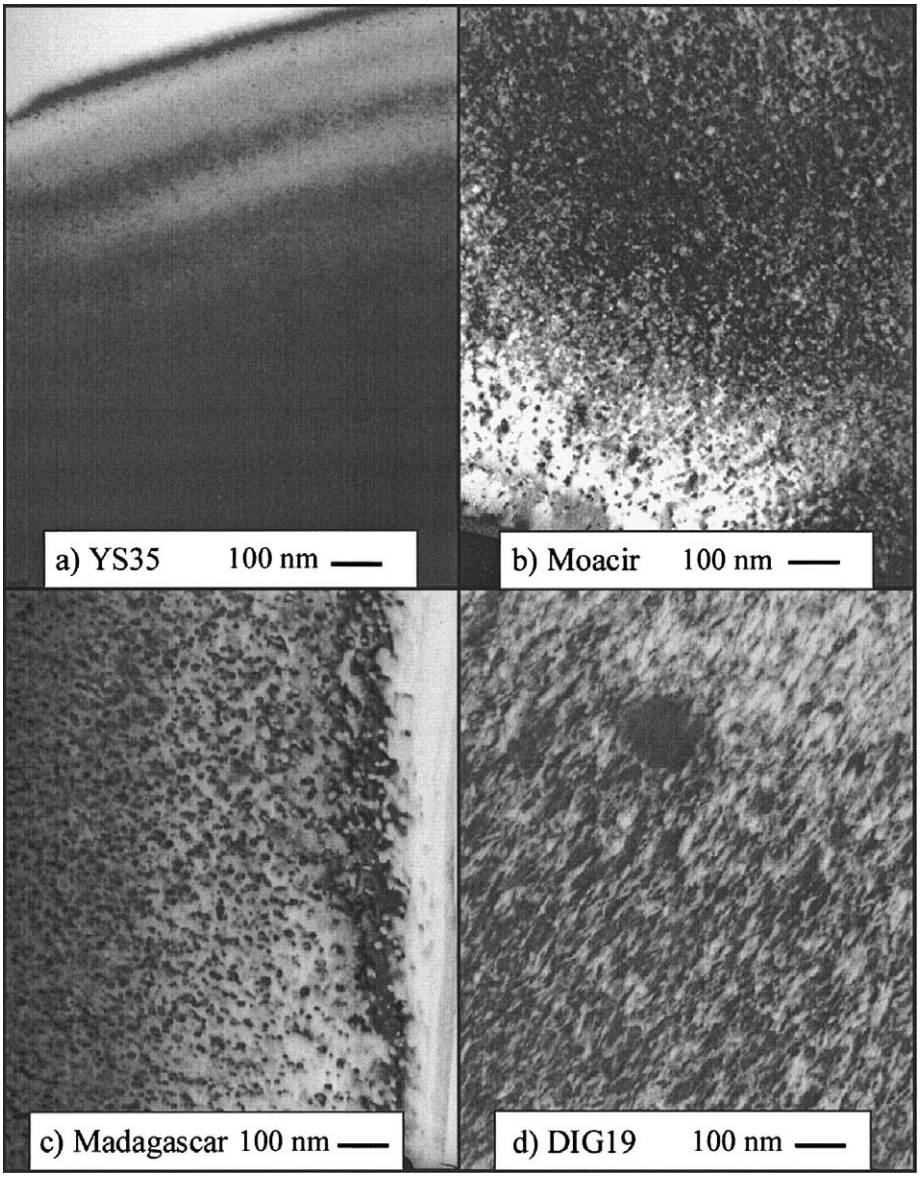

Fig. 3. Transmission Electron Microscope (TEM) Bright Field (BF) images of the four monazites. Note the gradual evolution of the mottled diffraction contrasts that are related to defects in the structure, with the increasing dose (from a to d). Initially the increasing amount of these areas (from YS35 to Moacir) is more important, than the increase in size.

5. DISCUSSION

5.1. Interpretation of the Results

In a recent study, Seydoux-Guillaume et al. (2002c) have demonstrated that the Moacir monazite is not a true "single crystal," as shown by the simple SAD pattern but consists of a mosaic of tiny (~5 nm^2), slightly distorted, domains that correspond to old defects induced by radioactive decay. These differences in orientation are responsible for the presence of (1) the mottled diffraction contrasts in the BF images, and (2) a second structural phase (B), which produces very broad reflections in the XRD patterns. Broadening of the B reflections is due to different degrees of distortion. In addition, the XRD pattern revealed that the rest of the monazite is a perfect "Phase A" monazite crystal but with expanded lattice caused by the accumulation of Helium.

Based on these observations on the Moacir monazite, Seydoux-Guillaume et al. (2002c) suggested that HRTEM images are not appropriate to highlight variable defect concentrations in monazites because the 25 nm^2 HRTEM images (Fig. 4) might not provide a representative sampling of the small number of distorted areas. In contrast, the XRD technique (Fig. 2) and TEM-BF images cover μm^2-sized areas (Fig. 3), allowing a clear distinction among various defect concentrations due to the larger amount of sample studied (i.e., a few mg for XRD). For setting up a classification scheme of self-irradiation-induced defect concentrations in monazites, we therefore recommend using XRD patterns and BF images. The HRTEM im-

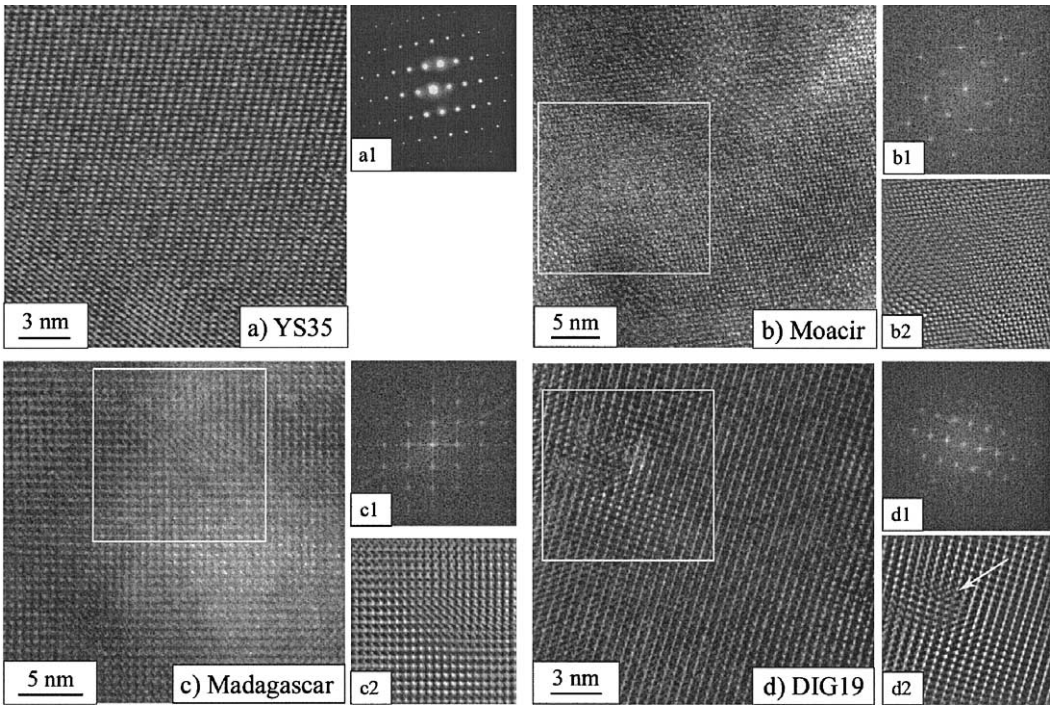

Fig. 4. Energy-filtered high resolution images (HRTEM) of the four monazites (a, b, c and d), with corresponding diffraction pattern (Fast Fourier Transform except for a1), and Inverse Fourier Transform of the area given by the box (b2, c2 and d2). The youngest monazite YS35 has a perfectly crystalline lattice, the others display small and distorted domains. The oldest DIG19 monazite shows edge dislocations (see the arrow in d2). None of the monazites is metamict.

ages, however, still provide two important pieces of information, namely, that the monazites are not amorphous (Fig. 4a1 to d1),, and that the defects are only nm-sized, localized, distorted areas (Fig. 4b2 to d2).

Both BF and HRTEM images revealed the almost perfectly crystalline lattice of monazite YS35. We infer that the corresponding XRD pattern should have very sharp reflections with a high intensity without shoulders, similar to a synthetic monazite (Seydoux-Guillaume et al., 2002a). As previously noted, the A-reflection maximum for the Madagascar monazite is shifted toward lower 2θ values as compared to that of the Moacir monazite. This can have either (1) a chemical or (2) a structural reason. In the first case, the different LREE, Th, U contents in the two monazites (Table 2) result in different lattice parameters, as demonstrated in many previous studies (e.g., Ni et al., 1995; Podor et al., 1995; Gratz and Heinrich, 1997; Podor and Cuney, 1997; Gratz and Heinrich, 1998; Seydoux-Guillaume et al., 2002a). The second explanation, proposed by Seydoux-Guillaume et al. (2002c) for the Moacir monazite, is that the lattice expansion is due to the presence of helium. As the Madagascar monazite has much higher Th and U contents than the Moacir monazite at approximately the same age, it contains more helium, probably causing the significant lattice expansion. Moreover, the Madagascar monazite was more affected by radiation damage, causing lattice distortion, which, in turn, results in a higher volume percentage of phase B (80 vol.%) as compared to the Moacir monazite (53 vol.%). On BF images, this is visualized by the increasing size of the mottled diffraction contrasts (Fig. 3b and c). In the case of monazite that received the highest dose, DIG19, XRD yields only the broad reflection B (Fig. 2b) with an area percentage of ~100% (Table 3). This implies that the complete monazite was affected by radiation damage, resulting in the total distortion of the lattice. If undistorted, perfectly crystalline domains A are still present in monazite DIG19, they were not resolved by the XRD technique. The BF image of monazite DIG 19 (Fig. 3d) confirms this result: the mottled diffraction contrasts are very large and seem to affect the whole lattice.

Helium concentration data are only available for the Moacir and Madagascar monazites (Seydoux-Guillaume et al., 2002c; R. Pik, private communication): In both samples, the U-Th-He and U-Pb ages are concordant. This fact indicates that the rocks containing both these different monazites were never heated above the closure temperature for He in monazite, i.e., ~220°C (Farley and Stockli, 2002). Surprisingly, although both monazites must have stayed at such low temperatures for a long time, they contain only quite low defect concentrations induced by self-irradiation. Amorphous domains are absent, only some misoriented regions interpreted as old α-recoil tracks, have been found. Two explanations are possible: (a) either the lattice can heal at such low temperatures, in accordance with experimental data (Meldrum et al., 1996, 1997, 2000; Ewing and Wang, 2002), or (b) ionization created by α-particles, or electrons from α-decay in the U and Th decay chains partially anneal structural damages created by the recoil of nuclei (Ouchani et al., 1997; Ewing and Wang, 2002; Harrison et al., 2002). Future experimental studies should focus on the healing mechanisms of monazite.

To conclude, this study demonstrates that despite the high self-irradiation doses of up to 17×10^{19} α-decay/g, none of the

monazite samples is metamict. Lattice distortion only occurred in nm-sized isolated domains. Even the high defect concentration featured in the 1.9 Ga monazite DIG19, in which the lattice is totally distorted, was insufficient to open and disturb the U-Th-Pb decay systems in these crystals. Although this defect concentration seems to be very high for a monazite, much higher defect concentrations occur in zircon, in which amorphous domains are very common. Finally, to answer our questions, it was demonstrated that the phenomenon described by Seydoux-Guillaume et al. (2002c), i.e., the presence of two different structural phases in monazite, of which one is distorted, is also observed in other monazites. The correlation between these "B domains" and the self-irradiation dose received by a monazite is a major outcome of this study.

5.2. Implications for Geochronology

The present study confirms that radiation damages, in the form of amorphous domains, do not accumulate in monazite because defects heal faster by self-annealing than the lattice is damaged. The only memory of self-irradiation induced defects in the monazites is the presence of the distorted domains. These domains are visible using TEM and correspond to the "B-phase" observed in XRD. Taking this observation together with results from diffusion experiments (e.g., Smith and Giletti 1997; Cherniak et al., 2000, 2002), and dating results showing that the U-Pb clock is resistant to temperatures exceeding 800–850°C (e.g., Copeland et al., 1988; De Wolf et al., 1993; Bingen and van Breemen, 1998; Kalt et al., 2000; Montel et al., 2000), we conclude that radiogenic Pb does not diffuse out of monazite grains at geologically measurable rates. Moreover, Montel et al. (2002) have shown that Pb fits very well in the monazite lattice, occupying probably the same structural site as the parent elements U and Th. This argument helps to understand why lead is obviously fixed quite well in the monazite lattice. Therefore, it is quite improbable that the diffusivity of Pb is enhanced due to the presence of radiation damage (see also Seydoux-Guillaume et al. (2003)). The combination of all these arguments explains why isotopic dating of monazite mostly yields concordant U-Pb ages. Furthermore, it is highly unlikely that monazite U-Pb ages represent "cooling ages."

5.3. Implications for Nuclear Waste Deposit Strategies

The results of this study have certain implications for the storage of nuclear waste. Natural minerals such as monazite are a great tool to test the long-term behaviour of waste-form phases in specific geological environments (e.g., Ewing and Wang, 2002). Monazite has already been proposed for use in single-phase ceramics to immobilize actinides (Boatner and Sales, 1988): natural monazite contains large amounts of $LREE^{3+}$, U^{4+}, and Th^{4+} (van Emden et al., 1997), for which the actinides Am^{3+}, Cm^{3+}, Np^{4+}, Pu^{4+} are good substitutes. Another reason concerns a property of monazite featured in this study, i.e., their mostly concordant U-Pb ages despite high self-irradiation doses over a long period of time. In the case of monazite DIG 19, for example, the U-Pb system remained closed for nearly 2 billion yrs. Therefore, monazite ceramics seem to be good candidates for the immobilization of high-level nuclear waste, as it may be able to retain actinides within its lattice for very long periods of time. It is, however, essential to point out the limitations of the current study. Precise data on the temperature and duration of the annealing of the investigated monazites are not available. Therefore, the timing of the development of the observed domain structures remains unconstrained. Moreover, our observations provide no insight into the annealing mechanisms (temperature, ionization?) of these defect structures. Future experiments should focus on determining possible annealing mechanisms in both doped and natural monazites. Other aspects that are of interest for nuclear waste deposit strategies are solubility, dissolution, doping, and charge balancing of the ceramics. Further studies under a variety of physical conditions are necessary to better understand the behaviour of such monazite-ceramics in aqueous solutions (Poitrasson et al., 2002). It should be the final aim of all these studies to construct models that allow the prediction of the structural state of monazite-type phases at a given time.

Acknowledgments—This work was supported by German Science Foundation (DFG) grant De 401/18–1. We appreciate technical assistance by F. Bartschat, T. Grund, U. Heitmann (Münster), O. Appelt, I. Bauer, K. Paech, and D. Rhede (GFZ-Potsdam). We are indebted to R. Pik (CRPG Nancy) for making unpublished He data available. Many thanks for M. Marinho (UFBA, Brazil) and F. Gibert (UBP-Clermont-Ferrand, France) who provided two of the samples. Constructive comments from three anonymous reviewers and associate editor Y. Amelin were appreciated. Thanks to E. Scherer for correcting the English language.

Associate editor: Y. Amelin

REFERENCES

Bingen B. and van Breemen O. (1998) U-Pb monazite ages in amphibolite- to granulite-facies orthogneiss reflect hydrous mineral breakdown reactions: Sveconorwegian Province of SW Norway. *Contrib. Mineral. Petrol.* **132,** 336–353.

Black L. P., Fitzgerald J. D., and Harley S. L. (1984) Pb isotopic composition, colour, and microstructure of monazites from a polymetamorphic rock in Antarctica. *Contrib. Mineral. Petrol.* **85,** 141–148.

Boatner L. A. and Sales B. C. (1988) Monazite. In *Radioactive Waste Forms for the Future* (eds. W. Lutze and R. C. Ewing) pp. 495–564. North Holland, Amsterdam.

Boatner L. A., Beall G. W., Abraham M. M., Finch C. B., Huray P. G. and Rappaz M. (1980) Monazite and other lanthanide orthophosphates as alternate actinide waste forms. In *Scientific Basis for Nuclear Waste Management* (ed. CJM Northrop Jr.) 2, pp. 289–296, Plenum Press.

Cherniak D. J. (1993) Lead diffusion in titanite and preliminary results on the effect of radiation damage on Pb transport. *Chem. Geol.* **110,** 177–194.

Cherniak D. J., Watson E. B., Harrison T. M. and Grove M. (2000) Pb diffusion in monazite: A progress report on a combined RBS/SIMS study. *EOS Trans. AGU.* **81,** Spring Meeting Supplement, S25.

Cherniak D. J., Watson E. B., Grove M. and Harrison T. M. (2002) Pb diffusion in monazite. *GSA Denver Annual Meeting,* A209.

Cocherie A., Legendre O., Peucat J. J., and Kouamelan A. N. (1998) Geochronology of polygenetic monazites constrained by in situ electron microprobe Th-U-total lead determination: implications for lead behaviour in monazite. *Geochim. Cosmochim. Acta* **62,** 2475–2497.

Copeland P., Parrish R. R. and Harrison T. M. (1988) Identification of inherited radiogenic Pb in monazite and its implication for U-Pb systematics. *Nature* **333,** 760–763.

Corfu F. (1988) Differential response of U-Pb systems in coexisting accessory minerals, Winnipeg River Subprovince, Canadian Shield: implications for Archean crustal growth and stabilization. *Contrib. Mineral. Petrol.* **98,** 312–325.

Cruz M. J., Cunha J. C., Merlet C. and Sabaté P. (1996) Datação pontual das monazitas da região de Itambé, Bahia, através da microssonda electrônica. *XXXIX Congresso Brasileiro de Geologia*. 206–209.

Davis D. W. and Krogh T. E. (2000) Preferential dissolution of 234U and radiogenic Pb from α-recoil-damaged lattice sites in zircon: implications for thermal histories and Pb isotopic fractionation in the near surface environment. *Chem. Geol.* **172,** 41–58.

De Wolf C. P., Belshaw N., and O'Nions R. K. (1993) A metamorphic history from micron-scale $^{207}Pb/^{206}Pb$ chronometry of Archean monazite. *Earth Planet. Sci. Lett.* **120,** 207–220.

Dodson M. H. (1973) Closure temperature in cooling geochronological and petrological systems. *Contrib. Mineral. Petrol.* **40,** 257–259.

Ewing R. C. (1975) The crystal chemistry of complex niobium and tantalum oxides. IV. The metamict state: Discussion. *Am. Mineral.* **60,** 728–733.

Ewing R. C., Weber W. J., and Clinard F. W., Jr.. (1995) Radiation effects in nuclear waste forms. *Progress Nucl. Energy* **29,** 63–127.

Ewing R. C., Meldrum A., Wang L. M. and Wang S. X. (2000) Radiation-Induced Amorphization. In *Reviews in Mineralogy and Geochemistry* (ed. P. H. Ribbe) 39, pp. 319–361. Mineralogical Society of America.

Ewing R. C. and Wang L. M. (2002) Phosphates as Nuclear Waste Forms. In *Reviews in Mineralogy and Geochemistry* (ed. P. H. Ribbe) 48, pp. 673–699. Mineralogical Society of America.

Farley K. A. and Stockli D. F. (2002) (U-Th)/He Dating of Phosphates: Apatite, Monazite and Xenotime. In *Reviews in Mineralogy and Geochemistry* (ed. P. H. Ribbe) 48, pp. 559–577. Mineralogical Society of America.

Förster H. J. (1998) The chemical composition of REE-Y-Th-U-rich accessory minerals in peraluminous granites of the Erzgebirge-Fichtelgebirge region, Germany, Part I: The monazite-(Ce)-brabantite solid solution series. *Am. Mineral.* **83,** 259–272.

Geisler T., Pidgeon R. T., van Bronswijk W., and Kurtz R. (2002) Transport of uranium, thorium, and lead in metamict zircon under low-temperature hydrothermal conditions. *Chem. Geol.* **191,** 141–154.

Goncalves P. (2002) Pétrologie et géochronologie des granulites de Ultra-Hautes Temperatures de l'unité basique d'Andriamena (Centre-Nord Madagascar). Apport de la géochronologie in-situ U-Th-Pb à l'interprétation des trajets P-T. Thèse de doctorat, Université Blaise-Pascal, Clermont-Ferrand, France, pp. 319.

Gratz R. and Heinrich W. (1997) Monazite-xenotime thermobarometry: experimental calibration of the miscibility gap in the binary system CePO4-YPO4. *Am. Mineral.* **82,** 772–780.

Gratz R. and Heinrich W. (1998) Monazite-xenotime thermobarometry. III. Experimental calibration of the partitioning of Gd between monazite and xenotime. *Eur. J. Mineral.* **10,** 579–588.

Harrison T. M., Catlos E. and Montel J. M. (2002) U-Th-. Pb dating of phosphate minerals. In *Reviews in Mineralogy and Geochemistry* (ed. P. H. Ribbe) 48, pp. 523–558. Mineralogical Society of America.

Holland H. D. and Gottfried D. (1955) The effect of nuclear radiation on the structure of zircon. *Acta Crystallogr.* **8,** 291–300.

Kalt A., Corfu F., and Wijbrans J. R. (2000) Time calibration of a P-T path from a Variscan high-temperature low-pressure metamorphic complex (Bayerische Wald, Germany), and the detection of inherited monazite. *Contrib. Mineral. Petrol.* **128,** 143–163.

Köppel V. (1974) Isotopic ages of monazites and zircons from the crust-mantle transition and adjacent units of the Ivrea and Ceneri zones (Southern Alps, Italy). *Contrib. Mineral. Petrol.* **43,** 55–70.

Krohe A. and Wawrzenitz N. (2000) Domainal variations of U-Pb monazite ages and Rb-Sr whole-rock dates in polymetamorphic paragneisses (KTB Drill Core, Germany): influence of strain and deformation mechanisms on isotope systems. *J. Metamorphic Geol.* **18,** 271–291.

Landzirotti A. and Hanson G. N. (1995) U-Pb dating of major and accessory minerals formed during metamorphism and deformation of metapelites. *Geochim. Cosmochim. Acta* **59,** 2513–2526.

Larson A. C. and Von Dreele R. B. (1988) GSAS-Generalized structure analysis system. *Los Alamos National Laboratory Report* LAUR 86–758: pp 223.

Leloup P. H., Lacassin R., Tapponnier P., Schärer U., Zhong Dalai, Liu Xiaohan, Zhang Linasheng, Shaocheng Ji, and Phan Trong Trinh (1995) The Ailao Shan-Red River shear zone (Yunnan, China), Tertiary transform boundary of Indochina. *Tectonophysics* **251,** 3–84.

Meldrum A., Wang L. M., and Ewing R. C. (1996) Ion-beam-induced amorphization of monazite. *Nucl. Instr. Meth. Phys. Res.* **B116,** 220–224.

Meldrum A., Boatner L. A., and Ewing R. C. (1997) Electron-irradiation-induced nucleation and growth in amorphous LaPO4, ScPO4, and zircon. *J. Mater. Res.* **12,** 1816–1827.

Meldrum A., Boatner L. A., Weber W. J., and Ewing R. C. (1998) Radiation damage in zircon and monazite. *Geochim. Cosmochim. Acta* **62,** 2509–2520.

Meldrum A., Boatner L. A., and Ewing R. C. (2000) A comparison of radiation effects in crystalline ABO4-type phosphates and silicates. *Mineral. Mag.* **64,** 183–192.

Montel J. M., Foret S., Veschambre M., Nicollet C., and Provost A. (1996) Electron microprobe dating of monazite. *Chem. Geol.* **131,** 37–53.

Montel J. M., Kornprobst J., and Vielzeuf D. (2000) Preservation of old U-Th-Pb ages in shielded monazite: example from the Beni Bousera Hercynian kinzigites (Morocco). *J. Metamorphic Geol.* **18,** 335–342.

Montel J. M., Devidal J. L., and Avignant D. (2002) X-ray diffraction study of brabantite-monazite solid solutions. *Chem. Geol.* **191,** 89–104.

Murakami T., Chakoumakos B. C., Ewing R. C., Lumpkin G. R., and Weber W. J. (1991) Alpha-decay event damage in zircon. *Am. Mineral.* **76,** 1510–1532.

Nasdala L., Pidgeon R. T., and Wolf D. (1996) Heterogeneous metamictization of zircon on a microscale. *Geochim. Cosmochim. Acta* **60,** 1091–1097.

Nasdala L., Wenzel M., Vavra G., Irmer G., Wenzel T., and Kober B. (2001) Metamictisation of natural zircon: Accumulation versus thermal annealing of radioactivity-induced damage. *Contrib. Mineral. Petrol.* **141,** 125–144.

Nasdala L., Lengauer C. L., Hanchar J. M., Kronz A., Wirth R., Blanc P., Kennedy A. K., and Seydoux-Guillaume A. M. (2002) Annealing radiation damage and the recovery of cathodoluminescence. *Chem. Geol.* **191,** 121–140.

Ni Y., Hughes J. M., and Mariano A. N. (1995) Crystal chemistry of the monazite and xenotime structures. *Am. Mineral.* **80,** 21–26.

Oelkers E. H. and Poitrasson F. (2002) An experimental study of the dissolution stoichiometry and rates of a natural monazite as a function of temperature from 50 to 230°C and pH from 1.5 to 10. *Chem. Geol.* **191,** 73–87.

Ouchani S., Dran J. C., and Chaumont J. (1997) Evidence of ionization annealing upon helium-ion irradiation of pre-damaged fluoroapatite. *Nucl. Instr. Meth. Phys. Res.* **B132,** 447–451.

Paquette J. L., Nedelec A., Moine B., and Rakotondrazafi M. (1994) U-Pb, Single Zircon Pb-Evaporation, and Sm/Nd Isotopic Study of a granulite domain in SE Madagascar. *J. Geol.* **102,** 523–538.

Paquette J. L., Montel J. M., and Chopin C. (1999) U-Th-Pb dating of the Brossasco ultrahigh-pressure metagranite, Dora-Maira massif, Western Alps. *Eur. J. Mineral.* **11,** 69–77.

Paquette J. L., Goncalves P., Devouard B. and Nicollet C. (2003) In situ ID-TIMS U-. Pb dating of single monazites: A new method to unravel complex poly-metamorphic evolutions. Application to the UHT granulites of Andriamena (North-Central Madagascar). *Contrib. Mineral. Petrol.* **147,** 110–122.

Parrish R. R. (1990) U-Pb dating of monazite and its application to geological problems. *Can. J. Earth Sci.* **27,** 1431–1450.

Parrish R. R. (1995) Thermal evolution of the southeastern Canadian Cordillera. *Can. J. Earth Sci.* **32,** 1618–1642.

Podor R. and Cuney M. (1997) Experimental study of Th-bearing LaPO4 (780°C, 200 MPa): implications for monazite and actinide orthophosphate stability. *Am. Mineral.* **82,** 765–771.

Podor R., Cuney M., and Nguyen Trung C. (1995) Experimental study of the solid solution between monazite-(La) and (Ca0.5U0.5)PO4 at 780°C and 200 MPa. *Am. Mineral.* **80,** 1261–1268.

Poitrasson F., Chenery S., and Bland D. J. (1996) Contrasted monazite hydrothermal alteration mechanisms and their geochemical implica-

tions for the U-Th-Pb geochronology and nuclear ceramics. *Earth Planet. Sci. Lett.* **145,** 79–96.

Poitrasson F., Chenery S., and Shepherd T. J. (2000) Electron microprobe and LA-ICP-MS study of monazite hydrothermal alteration: implications for the U-Th-Pb geochronology and nuclear ceramics. *Geochim. Cosmochim. Acta* **64,** 3283–3297.

Poitrasson F., Hanchar J. M., and Schaltegger U. (2002) The current state and future of accessory mineral research. *Chem. Geol.* **191,** 3–24.

Read D. and Williams C. T. (2001) Degradation of phosphatic waste forms incorporating long-lived radioactive isotopes. *Miner. Mag.* **65,** 589–601.

Romer R. (2003) Alpha-recoil in U-. Pb geochronology: effective sample size matters. *Contrib. Mineral. Petrol.* **145,** 481–491.

Salje E. K. H. (2000) Structural transformations in minerals: The role of temperature and radiation damage. *Berichte der Deutschen Mineralogischen Gesellschaft, Beihefte Eur. J. Miner.* **12,** 175.

Schärer U. and Deutsch A. (1990) Isotope systematics and shock-wave metamorphism: II. U-Pb and Rb-Sr in naturally shocked rocks; the Haughton Impact Structure, Canada. *Geochim. Cosmochim. Acta* **54,** 3435–3447.

Schärer U., Xu R. H., and Allègre C. J. (1986) U-(Th)-Pb systematics and ages of Himalayan leucogranites, South Tibet. *Earth. Plan. Sci. Lett.* **77,** 35–48.

Schärer U., Zhang L. S., and Tapponnier P. (1994) Duration of strike-slip movements in large shear zones: the Red River belt, China. *Earth Planet. Sci. Lett.* **126,** 379–397.

Seydoux-Guillaume A. M., Wirth R., Heinrich W., and Montel J. M. (2002a) Experimental determination of the Th partitioning between monazite and xenotime using Analytical Electron Microscopy and X-ray Diffraction Rietveld analysis. *Eur. J. Mineral.* **14,** 869–878.

Seydoux-Guillaume A. M., Paquette J. L., Wiedenbeck M., Montel J. M., and Heinrich W. (2002b) Experimental resetting of the U-Th-Pb system in monazite. *Chem. Geol.* **191,** 165–181.

Seydoux-Guillaume A. M., Wirth R., Nasdala L., Gottschalk M., Montel J. M., and Heinrich W. (2002c) An XRD, TEM and Raman study of experimentally annealed natural monazite. *Phys. Chem. Miner.* **29,** 240–253.

Seydoux-Guillaume A. M., Goncalves P., Wirth R., and Deutsch A. (2003) TEM study of polyphasic discordant monazites: site specific specimen preparation by using the Focused Ion Beam technique. *Geol.* **31,** 973–976.

Smith H. A. and Barreiro B. (1990) Monazite U-Pb dating of staurolite grade metamorphism in pelitic schists. *Contrib. Mineral. Petrol.* **105,** 602–615.

Smith H. A. and Giletti B. J. (1997) Lead diffusion in monazite. *Geochim. Cosmochim. Acta* **61,** 1047–1055.

Suzuki K. and Adachi M. (1994) Middle Precambrian detrital monazite and zircon from the Hida gneiss on Oki-Dogo Island, Japan: their origin and implications for the correlation of basement gneiss of Southwest Japan and Korea. *Tectonophysics* **235,** 277–292.

Suzuki K., Adachi M., and Kajizuka I. (1994) Electron microprobe observations of Pb diffusion in metamorphosed detrital monazites. *Earth Plan. Sci. Lett.* **128,** 391–405.

Teufel S. and Heinrich W. (1997) Partial resetting of the U-Pb isotope system in monazite through hydrothermal experiments: an SEM and U-Pb isotope study. *Chem. Geol.* **137,** 273–281.

Trachenko K., Dove M. T., and Salje E. K. H. (2000) Modelling the percolation-type transition in radiation damage. *J. Appl. Phys.* **87,** 7702–7707.

van Emden B., Thornber M. R., Graham J., and Lincoln F. J. (1997) The incorporation of actinides in monazite and xenotime from placer deposits in western Australia. *Can. Mineral.* **35,** 95–104.

Villa I. (2002) Where is geochronology going? Alteration and mineral mixtures. *Geochim. Cosmochim. Acta* **66,** S1., A807.

Weber W. J., Ewing R. C., Catlow C. R. A., Diaz de la Rubia T., Hobbs L. W., Kinishita C., Matzke H. J., Motta A. T., Nastasi M., Salje E. H. K., Vance E. R., and Zinkle S. J. (1998) Radiation effects in crystalline ceramics for the immobilization of high-level nuclear waste and plutonium. *J. Mater. Res.* **13,** 1434–1484.

Zhang L.-S. and Schärer U. (1999) Origin and age of magmatism along the Red River shear belt, Yunnan, China. *Contrib. Mineral. Petrol.* **134,** 67–85.